REINFORCING NEURON EXTRACTION FROM CALCIUM IMAGING DATA VIA DEPTH-ESTIMATION CONSTRAINED NONNEGATIVE MATRIX FACTORIZATION (SUPPLEMENTARY MATERIAL)

Peixian Zhuang, Jiamin Wu ✉

Department of Automation, Tsinghua University, Beijing, China
Institute for Brain and Cognitive Science, Tsinghua University, Beijing, China
✉ wujiamin@tsinghua.edu.cn.

ABSTRACT

This supplementary material provides the proof of our depth-dependent transmission estimation model Eq. (2), numerical solutions to the three sub-problems (4)-(6), and more experimental results.

1. PROOF OF EQ. (2).

The dichromatic atmospheric scattering model [1] has been widely used in image descattering, and an observed image $\mathbf{I}$ can be seen as an additive combination of attenuation $\mathbf{E}_a$ and airlight $\mathbf{E}_l$:

$$\begin{aligned}\mathbf{I} &= \mathbf{E}_a + \mathbf{E}_l, \\ &= \mathbf{E}_\infty \boldsymbol{\rho} e^{-\beta \mathbf{d}} + \mathbf{E}_\infty (1 - e^{-\beta \mathbf{d}}),\end{aligned} \tag{1}$$

where $\mathbf{E}_\infty$ is the airlight radiance, $\boldsymbol{\rho}$ and $\mathbf{d}$ are the scene albedo and depth at the scene point. The attenuation coefficient β is seen as a constant. $\mathbf{t} = e^{-\beta \mathbf{d}}$ is the depth-dependent transmission that has been widely used in most image descattering methods.

It is assumed that the radiance of environmental illumination of both attenuation and airlight is approximately equal in local pixels, and $\mathbf{A} = \mathbf{E}_\infty$ denotes the environmental illumination for convenience. The scattering model Eq. (1) is refined:

$$\mathbf{I} = \mathbf{A}\boldsymbol{\rho}\mathbf{t} + \mathbf{A}(1 - \mathbf{t}), \tag{2}$$

In the case of dark channel, $\boldsymbol{\rho}^{dark}(x) = 0$,

$$\begin{aligned}\mathbf{I}^{dark}(x) &= \mathbf{A}(x)\boldsymbol{\rho}^{dark}(x)\mathbf{t}(x) + \mathbf{A}(x)(1 - \mathbf{t}(x)), \\ &= \mathbf{A}(x)(1 - \mathbf{t}(x)),\end{aligned} \tag{3}$$

In the case of bright channel, $\boldsymbol{\rho}^{bright}(x) = 1$,

$$\begin{aligned}\mathbf{I}^{bright}(x) &= \mathbf{A}(x)\boldsymbol{\rho}^{bright}(x)\mathbf{t}(x) + \mathbf{A}(x)(1 - \mathbf{t}(x)), \\ &= \mathbf{A}(x),\end{aligned} \tag{4}$$

where $\mathbf{I}^{dark}$ and $\mathbf{I}^{bright}$ are the dark channel [2] and the bright channel [3] of $\mathbf{I}$, respectively. To eliminate artifact effects due to image patch-based operation, a prevailing guided image filtering [4] is linearly implemented to refine $\mathbf{I}^{dark}$ and $\mathbf{I}^{bright}$ respectively. Based on Eqs. (3) and (4), we deduce the solution of the transmission:

$$\mathbf{t}(x) = 1 - \frac{\mathbf{I}^{dark}(x)}{\mathbf{I}^{bright}(x)}, \tag{5}$$

To avert the similar phenomenon of *aerial perspective* [2], we introduce an empirical weight coefficient ω into Eq. (5) for avoiding transmission overestimation. Hence, the proof of Eq. (2) in the main text is completed.

2. SOLUTION TO THREE SUB-PROBLEMS (4)-(6).

We update to solve the three sub-problems (4)-(6) of the main text in an alternating fashion. Optimization details are summarized below:

First, we perform the updating algorithm for solving (4) of the main text that has been similarly presented in [5, 6], and the optimization algorithm is modified from fastHALS [7]. Since $\mathbf{P}$ focuses on the fluctuating signals and its estimation is independent of $\mathbf{b}_0$, we first estimate $\mathbf{P}$ and then update the closed-form solution $\mathbf{b}_0 = \frac{1}{N}(\tilde{\mathbf{Y}} - \mathbf{P} \cdot \mathbf{C}) \cdot \mathbf{1}$. The updating algorithm is sketched in **Algorithm 1**.

Algorithm 1 Solution to (4) in the main text

function update_spatial_footprint $(\tilde{\mathbf{Y}}, \mathbf{P}, \mathbf{C}, \mathbf{D}, \mathbf{F}, \mathbf{b}_0)$
$\mathrm{U} \leftarrow (\tilde{\mathbf{Y}} - \mathbf{D} \cdot \mathbf{F} - \mathbf{b}_0 \cdot \mathbf{1}^T) \cdot \mathbf{C}^T$
$\mathrm{V} \leftarrow \mathbf{C} \cdot \mathbf{C}^T$
for $i = 1, ..., N$ **do**
  for $k = 1, ..., K$ **do**
    $\mathbf{p}_k \leftarrow \max(0, \mathbf{p}_k + \frac{\mathbf{u}_k - \mathbf{P} \cdot \mathbf{v}_k}{\mathbf{v}_{kk}})$
  end for
end for
$\mathbf{b}_0 \leftarrow \frac{1}{N}(\tilde{\mathbf{Y}} - \mathbf{P} \cdot \mathbf{C}) \cdot \mathbf{1}$
return $\mathbf{P}$ and $\mathbf{b}_0$

Second, we adopt the similar algorithm of [5, 6] for addressing (5) of the main text by updating all neurons and computing the unconstrained estimate of each neuron. We deconvolve and denoise the noisy estimate ($\tilde{\mathbf{y}}_i = \mathbf{c}_i + \frac{\mathbf{p}_i^T \cdot \tilde{\mathbf{Y}}_{res}}{\mathbf{p}_i^T \cdot \mathbf{p}_i}$) to generate the temporal trace $\mathbf{c}_i$ and the spike signal $\mathbf{s}_i$. While $\mathbf{C}$ is estimated, we update $\mathbf{b}_0$ by the closed-form solution $\mathbf{b}_0 = \frac{1}{N}(\tilde{\mathbf{Y}} - \mathbf{P} \cdot \mathbf{C}) \cdot \mathbf{1}$. The summary of the updating algorithm is described in **Algorithm 2**.

Algorithm 2 Solution to (5) in the main text

function update_temporal_trace $(\tilde{\mathbf{Y}}, \mathbf{P}, \mathbf{C}, \mathbf{D}, \mathbf{F}, \mathbf{b}_0)$
$\mathrm{U} \leftarrow \mathbf{P}^T \cdot (\tilde{\mathbf{Y}} - \mathbf{D} \cdot \mathbf{F} - \mathbf{b}_0 \cdot \mathbf{1}^T)$
$\mathrm{V} \leftarrow \mathbf{P}^T \cdot \mathbf{P}$
for $i = 1, ..., N$ **do**
  for $k = 1, ..., K$ **do**
    $(\mathbf{c}_k, \mathbf{s}_k) \leftarrow$ deconvolve_and_denoise$(\mathbf{c}_k + \frac{\mathbf{u}_k - \mathbf{v}_k \cdot \mathbf{C}}{\mathbf{v}_{kk}})$
  end for
end for
$\mathbf{b}_0 \leftarrow \frac{1}{N}(\tilde{\mathbf{Y}} - \mathbf{P} \cdot \mathbf{C}) \cdot \mathbf{1}$
return $\mathbf{C}$, $\mathbf{S}$ and $\mathbf{b}_0$

Last, the constraint in (6) of the main text spontaneously produces the same closed-form estimation above, then (6) degenerates into a standard singular value decomposition (SVD) problem and its solution corresponds to the top singular components of $(\tilde{\mathbf{Y}} - \mathbf{P} \cdot \mathbf{C} - \mathbf{b}_0 \cdot \mathbf{1}^T)$. The overview of the updating algorithm is depicted in **Algorithm 3**.

Algorithm 3 Solution to (6) in the main text

function update_background $(\tilde{\mathbf{Y}}, \mathbf{P}, \mathbf{C})$
$\mathbf{b}_0 \leftarrow \frac{1}{N}(\tilde{\mathbf{Y}} - \mathbf{P} \cdot \mathbf{C}) \cdot \mathbf{1}$
$[\mathbf{U}, \mathbf{\Sigma}, \mathbf{V}] \leftarrow \mathrm{SVD}(\tilde{\mathbf{Y}} - \mathbf{P} \cdot \mathbf{C} - \mathbf{b}_0 \cdot \mathbf{1}^T)$
$\mathbf{D} = \mathbf{U} \cdot \mathbf{\Sigma}$, $\mathbf{F} = \mathbf{V}^T$
return $\mathbf{D}$, $\mathbf{F}$ and $\mathbf{b}_0$

3. MORE EXPERIMENTAL RESULTS

Results of background suppression and noise removal. Fig. 1 exhibits comparative results of background suppression and denoising effect by CNMFE [5] and DCNMFE. The tendency is clear from the naive method CNMFE to our depth-estimation constraint nonnegative matrix factorization DCNMFE: background suppression results are more obvious, and denoising effects become more remarkable. Fig. 2 visualizes the results of headmost four neurons extracted by CNMF [8] and DCNMF in terms of background suppression and denoising effect. CNMF fails to demix spatially overlapping neurons and extract the headmost four neurons without depth estimation for alleviating image scattering. In contrast, DCNMF comprehensively outperforms CNMF over neuron extraction accuracy, neuron signal retention, background suppression, and denoising effect. These demonstrate a stable consistency with previous experimental results.

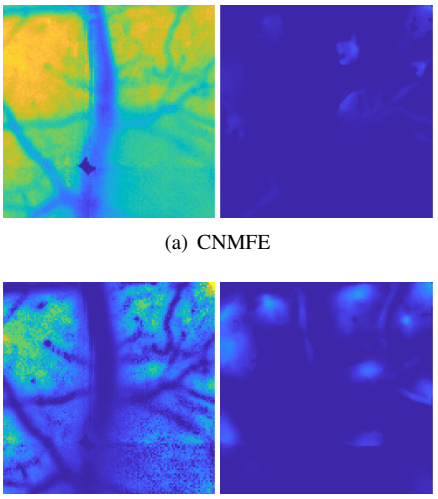

(a) CNMFE

(b) DCNMFE

Fig. 1: **Results of background suppression and denoising effect.** The tendency is clear from CNMFE [5] to DCNMFE: background is substantially suppressed in left-side columns, and denoising effect becomes more remarkable in right-side columns.

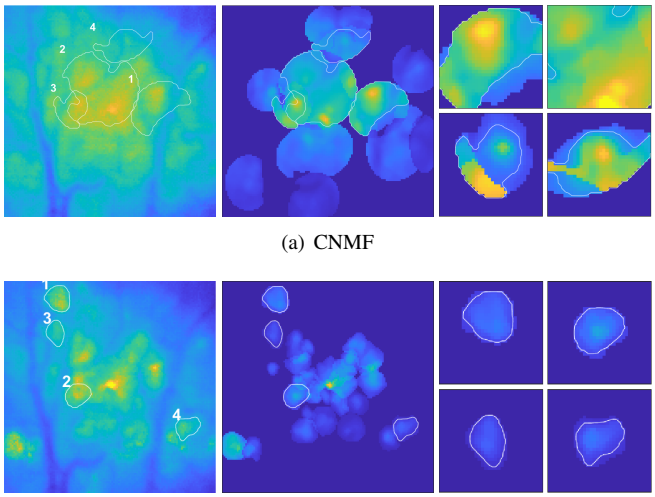

(a) CNMF

(b) DCNMF

Fig. 2: **Results of headmost four neurons extracted by CNMF [8] and DCNMF.** DCNMF outperforms CNMF in terms of neuron extraction accuracy (rightmost column), background suppression (leftmost column), neuron retention and denoising effect (middle column). The comparative video results can be available at https://github.com/zhuangpeixian/DCNMFE.

Results of surgical image descattering. We use our transmission estimation Eq. (2) in the main text instead of the transmission estimation based on dark channel prior, and then

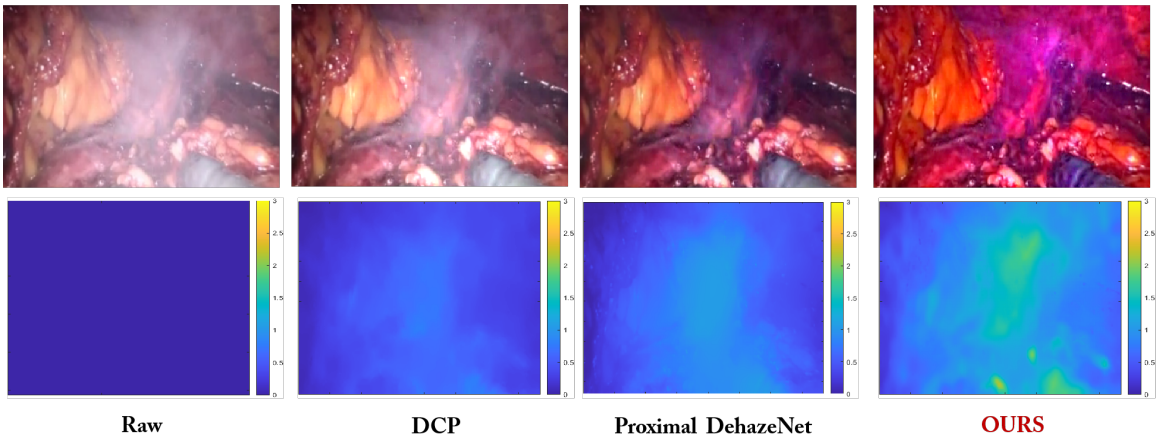

Fig. 3: **Results of surgical image descattering.** Compared with DCP [2] and Proximal DehazeNet [9] that use constant atmospheric light, our method exhibits better descattering results (top row) and yields more accurate depth estimations (bottom row).

obtain final dehazed images via solving dichromatic atmospheric light scattering model [2]. As shown in Fig. 3, compared with DCP [2] and Proximal DehazeNet [9] that adopt constant atmospheric light, our method (OURS) shows better descattering results and yields more accurate results of depth estimation. This suggests the validity of our depth-estimation model in image descattering.

4. REFERENCES

[1] S.G. NarasimhanShree, K. Nayar, "Vision and the atmosphere," *International Journal of Computer Vision*, vol. 48, no. 3, pp. 233-254, 2002.

[2] K. He, J. Sun, X. Tang, "Single image haze removal using dark channel prior," *IEEE Computer Conference on Computer Vision and Pattern Recognition (CVPR)*, 2009, pp. 1956-1963.

[3] Y. Yan, W. Ren, Y. Guo, R. Wang, X. Cao, "Image deblurring via extreme channels prior," *IEEE Computer Conference on Computer Vision and Pattern Recognition (CVPR)*, 2017, pp. 4003-4011.

[4] K. He, J. Sun, X. Tang, "Guided image filtering," *IEEE Trans. Pattern Anal. Mach. Intell.*, vol. 35, no. 6, pp. 1397-1409, 2013.

[5] P. Zhou, S.L. Resendez, J. Rodriguez-Romaguera, J.C. Jimenez, S.Q. Neufeld, A. Giovannucci, J. Friedrich, E.A. Pnevmatikakis, G.D. Stuber, R. Hen, M.A. Kheirbek, B.L. Sabatini, R.E. Kass, L. Paninski, "Efficient and accurate extraction of in vivo calcium signals from microendoscopic video data," *Elife*, vol. 7, pp. e28728, 2018.

[6] P. Zhou, J. Reimer, D. Zhou, A. Pasarkar, I.A. Kinsella, E. Froudarakis, D. Yatsenko, P. Fahey, A. Bodor, J.Buchanan, D.J. Bumbarger, "EASE: EM-Assisted Source Extraction from calcium imaging data," *bioRxiv*, doi: 10.1101/2020.03.25.007468, 2020.

[7] A. Cichocki, A.H. Phan, "Fast local algorithms for large scale nonnegative matrix and tensor factorizations," *IEICE Transactions on Fundamentals of Electronics, Communications and Computer Sciences*, vol. E92-A, no. 3, pp. 708-721, 2009.

[8] E.A. Pnevmatikakis, D. Soudry, Y. Gao, T.A. Machado, J. Merel, D. Pfau, T. Reardon, Y. Mu, C. Lacefield, W. Yang, M. Ahrens, R. Bruno, T.M. Jessell, D.S. Peterka, R. Yuste, L. Paninski, "Simultaneous denoising, deconvolution, and demixing of calcium imaging data," *Neuron*, vol. 89, pp. 285-299, 2016.

[9] D. Yang, J. Sun, "Proximal Dehaze-Net: A prior learning-based deep network for single image dehazing," *European Conference on Computer Vision (ECCV)*, 2018, pp. 729-746.